

REFINEMENT ANALYSIS, PHOTOLUMINESCENCE AND MAGNETIC PROPERTIES OF $Zn_{1-x}Mn_xO$ ($x = 0.00, 0.01, 0.02, 0.03$ & 0.04) NANOPARTICLES SYNTHESIZED BY COMBUSTION TECHNIQUE

P. MUNIRAJA^a, K. S. KUMAR^a, A. SUDHARANI^a, M. RAMANADHA^a,
S. RAMU^a, R. P. VIJAYALAKSHMI^a, B. POORNAPRAKASH^{b*}

^aDepartment of Physics, Sri Venkateswara University, Tirupati- 517502, India

^bDepartment of Electronic Engineering, Yeungnam University, Gyeongsan-38541, South Korea

$Zn_{1-x}Mn_xO$ ($x = 0.0, 0.01, 0.02, 0.03$ & 0.04) nanoparticles were fabricated through a simple combustion method and their structural, morphological, chemical, optical, photoluminescence and magnetic properties were systematically analyzed. X-ray diffraction (XRD) and Rietveld refinement (RR) analysis studies divulged that, the synthesized nanoparticles exhibited the hexagonal structure without any impurity phase. Morphology studies revealed that the synthesized nanoparticles were nearly spherical in shape with uniform size distribution. A clear Blue shift was recognized in the ZnO nanoparticles when doped with Mn ions. The photoluminescence (PL) spectra of all the synthesized nanoparticles exhibited the same emissions and PL intensity diminished with increase in Mn doping concentration. All the synthesized nanoparticles exhibited room temperature ferromagnetism (RTFM) and $Zn_{1-x}Mn_xO(x=0.02)$ nanoparticles displayed better ferromagnetic property than other compositions. The captive properties of the ZnO: Mn nanoparticles may more useful for optoelectronic and spintronic applications.

(Received September 11, 2019; Accepted April 27, 2020)

Keywords: Zinc oxide, Photoluminescence, Ferromagnetism, Spintronics, Optoelectronics

1. Introduction

Currently, researchers have perceived that in several semiconductor crystals substituting of transition metal in host affix local magnetic moments to the system. The doped materials are entitled as dilute magnetic semiconductors (DMS) [1]. Theoretical explorations imply that the semiconductor with direct band gap is the most probable candidate for spintronic devices [2]. ZnO is an n-type II-VI semiconductor with characteristic features such as direct energy band gap of 3.37eV, large binding energy 60meV in addition to wurtzite structure at room temperature [3]. Properties of ZnO nanoparticles can be tailored by dopants and doping concentration [4]. The foremost challenge for the practical applications of DMS is the achievement of ferromagnetism (FM) at room temperature. Transition metal (TM) doped ZnO is one of the best auspicious DMS candidates as it is anticipated to be RTFM (Room Temperature Ferromagnetism). The most propitious property of DMS is that, the substitution of TM in semiconductors does not influence the crystal structure but dramatically switches its dielectric, magnetic and electrical/optical properties, i.e. RTFM is observed in TM doped ZnO [5-6]. The doped TMs are irregularly assigned to substitution lattice sites and ferromagnetic aligned via an indirect magnetic coupling [7]. The TM doped ZnO would be proper for a number of devices such as magnetic devices with gain, spin transistors operated at very low power for mobile applications, optical emitter with encoded information [8]. Some of the reports argued that the RTFM of TM doped metal oxides strongly depends on the metal oxide host system, size, defects, size, type of dopant and concentration [9]. Venkatesem et al. [10] observed the high magnetic moment in Co doped ZnO films. Stable FM ordering observed from carrier mediated exchange interactions for several TM doped ZnO DMS [11]. Among them, Mn doped ZnO would show FM above room temperature and may be applied to shortwave magneto optical devices [12]. Paramagnetism was observed in ZnO: Mn films

* Corresponding authors: mail2poorna6@gmail.com

prepared by magnetron sputtering [13], solid state reaction [14]. Fuluknave et al. [15] found a spin glass behavior. Low et al. [16] found an antiferromagnetism in Mn doped ZnO by combustion method. At the same time both ferromagnetism and the absence of ferromagnetism were noticed in TM doped ZnO thin films grown by Molecular Beam Epitaxy (MBE) [17]. Diet et al. [18] predicted that Mn doped ZnO should be FM at room temperature. In the absence of p-type doping Mn doped ZnO would be antiferromagnetic [19]. Ferromagnetic phase transition in Mn substituted ZnO was observed due to the existence of spinel impurity phase like M_2O_4 in the system [20]. Chen et al. [37] shown FM in Mn substituted ZnO by solid state reaction method calcinized in Ar gas. However it will disappear in samples calcinized in the air. The magnetic properties are strongly determined by several defects [21-23]. Different magnetic properties reported in TM doped ZnO are originated due the different preparation methods, and hence the magnetic properties of ZnO or TM doped ZnO are sensitive to synthesis conditions.

Various techniques like Thermal deposition, Co-precipitation, Salvo-thermal approach, Spray pyrolysis, CVD, Sol-gel method and hydrothermal etc. are available to synthesis of Pure ZnO and Mn doped ZnO nanoparticles [24-30]. Although combustion method is an unique to synthesize $Zn_{1-x}Mn_xO$ ($x = 0.0, 0.01, 0.02, 0.03$ & 0.04) nanoparticles, as it involves less time of reaction, low cost, uniform size and easy to operate in addition to achieve fine nanoparticles without further heat treatment. Moreover, a few papers were available on the combustion synthesis of pure and Mn doped ZnO nanoparticles. Hence, we have made an attempt to synthesize $Zn_{1-x}Mn_xO$ ($x = 0.0, 0.01, 0.02, 0.03$ & 0.04) nanoparticles through combustion method at different Mn concentrations and procured their structural, optical, photoluminescence and magnetic properties.

2. Experimental procedure and characterization techniques

2.1. Experimental procedure

$Zn_{1-x}Mn_xO$ ($x = 0.0, 0.01, 0.02, 0.03$ & 0.04) nanoparticles were successfully synthesized by simple combustion method at 500 °C. All the chemical reagents such as urea zinc nitrate, manganese acetate were taken in pure form without further purification. Appropriate proportions (1:5) of zinc nitrate (11.899 g) and urea (12.012 g) and solutions were prepared separately and to be stirred for 30 minutes. After that, urea solution was slowly added drop wise to zinc nitrate solution with help of burette while stirring. To this solution Ammonium hydroxide is then added till pH attained to 9. 2 mL of capping agent such as polyethylene glycol (PEG) was added and stirring is extended up to 7 hours. The resulting solution is kept at 500 °C temperature for 60 minutes. The obtained ZnO nanoparticles were then grinded for 30 minutes and annealed at 600 °C for 1 hour. Similarly $Zn_{1-x}Mn_xO$ ($x = 0.01, 0.02, 0.03$ & 0.04) nanoparticles were prepared in the same route.

2.2. Characterization techniques

Crystallite sizes and phase identification of $Zn_{1-x}Mn_xO$ ($x = 0.0, 0.01, 0.02, 0.03$ & 0.04) nanoparticles were analyzed by RINT-2000 X-ray diffractometer. Morphology studies were identified by FESEM operating at 15 KV and TEM operating at 100 KV. Elemental compositions were detected by EDS (Energy Dispersive X-ray analysis). Optical measurement such as band gap energy (E_g) was identified using a UV-Visible spectrometer in diffuse reflection spectra (DRS) at room temperature. Raman analysis was carried out in the interim of $150-1500$ cm^{-1} . Room temperature Photoluminescence (PL) data were recorded on Perkin Elmer Horiba model using Xe lamp having excitation wavelength of 425 nm. Room temperature Magnetic behaviour (M-H curve) was analyzed by vibrating sample magnetometer in the interval of ± 15 kG.

3. Results and discussions

3.1. XRD analysis

X-ray diffraction analysis was carried out to check the influence of Mn concentration on the phase composition and structural properties of $Zn_{1-x}Mn_xO$ ($x = 0.0, 0.01, 0.02, 0.03$ & 0.04) nanoparticles and depicted in the Fig.1. All the diffracted peaks are graded as (100), (002), (101), (102), (110), (103), (200), (112), (201) and (004), at the corresponding angles of 2θ values are $31.7, 34.3, 36.1, 47.6, 56.6, 62.5, 66.3, 67.8, 69.0,$ and 76.8° respectively, indicates the hexagonal wurtzite structure of ZnO corresponds to JCPDS No: 05-0664 [31]. No additional diffraction peaks were noticed in the XRD pattern indicates the formation of impurity free single phase. The maximum intensity peak (101) slightly shifted from 36.14 to 36.26° as the Mn concentration increases in the ZnO host, suggest that Mn^{+2} ions may occupy in interstitial sites or Zn^{+2} sites in the ZnO lattice without affecting the crystal structure. The average particle size was estimated from the broadening of most prominent (101) peak with well noticed Debye Scherrer's formula as

$$D = \frac{0.94\lambda}{\beta \cos\theta}$$

where D is the size of the particle, λ is the wavelength (1.541 \AA) of the X-ray, β is the full width at half maxima (FWHM) and θ is the diffraction angle.

The variation of particle size with Mn concentration in the ZnO host is tabulated in the Table 1. This indicates that, the size of the nanoparticles decreases from 37 to 19nm with increasing Mn percentage in the ZnO lattice. The right shift of (101) peak may be due to decreased particle size caused by a result of lattice contraction/strain in the ZnO lattice with incorporation of Mn^{+2} [23]. During the doping process some quantity of Mn^{+2} may locate in or on the zone boundary of ZnO NPs resulting decrease in diffusion rate, which prevents the growth of the crystal. Similar type of observations were noticed in TM doped ZnO [32-35]. The Rietveld refinement (RR) plot of ZnO nanoparticles are displayed in the Fig. 2 and the calculated patterns are shown in the same field as solid line curve. RR analysis was performed with EXPO-2014 software, and the observed microstructure parameters are listed in the Table 1.

The lattice parameter 'a' was calculated along (100) plane and is given by [36] $a = \frac{\lambda}{\sqrt{3}\sin\theta}$ and the lattice parameter 'c' along (002) plane [36] is given by $c = \frac{\lambda}{\sin\theta}$

The lattice parameters 'a' and 'c' are decreased with increasing Mn concentration causes decreased particle size and tabulated in the Table 1. The c/a parameter has also been found to show nearly agreement with the value of standard value of 1.633 for closed packed hexagonal structure. The unit cell volume was calculated from $V = 0.866 a^2 c$, and found decreases with Mn concentration in ZnO, tabulated in the Table 1, it may due to decreasing of lattice parameters 'a' and 'c'.

Atomic packing fraction (APF) was calculated from the formula as $APF = \frac{2\pi a}{3\sqrt{3}c}$

It is found that APF decreases with increasing Mn substitution may be due to the increment of voids in the samples.

The nearest neighbor Zn-O bond length along the 'c' direction

$$L = \sqrt{\frac{a^2}{3} + \left(\frac{1}{2} - u\right)^2 c^2}$$

Here 'a' and 'c' are the lattice parameters, u is the positional parameter for hexagonal wurtzite structure, it is a measure of the amount by which each atom is displaced with respect to the next along the 'c' axis.

$$\text{Internal/positional parameter (u)} = \frac{1}{3} \left(\frac{a^2}{c^2} \right) + \frac{1}{4}$$

The calculated Zn-O bond lengths were good greed with the reported Zn-O bond length in the unit cell of ZnO and neighboring atoms is 1.9767Å. The dislocation density (δ) [36], which represents the amount of defects present in the sample is defined as the length of dislocation lines per unit volume and is calculated using the formula as

$$\delta = \frac{1}{D^2},$$

where D is the crystallite size. The dislocation density increases with increasing Mn content and displayed in the Table 1.

The surface to volume ratio of nanoparticles was calculated from the equation as

$$\frac{Ns}{Nv} = \frac{S R_o}{V - S R_o} = \frac{3 R_o}{R - R_o}$$

where Ns and Nv stands for number of ZnO pairs at surface and volume respectively, S is the surface area, V is the volume, Ro is the ZnO distance (0.18 nm), R is the average particle size. The S/V value increases with Mn concentration may be due to decreased particle size. The strain-induced broadening in the peak due to crystal imperfection and distortion was calculated using the formula as $\text{strain } s = \frac{\beta}{4 \tan \theta}$

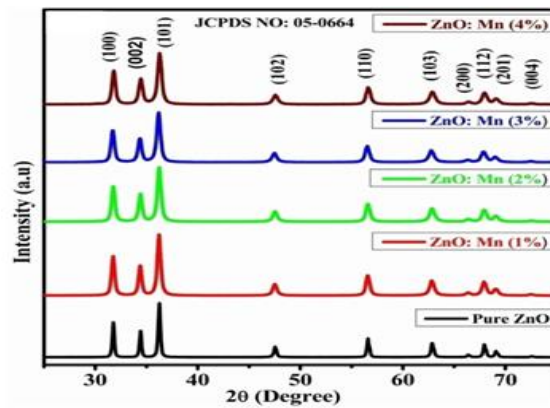


Fig. 1(a) XRD patterns of $Zn_{1-x}Mn_xO$ ($x = 0.0, 0.01, 0.02, 0.03$ & 0.04) nanoparticles

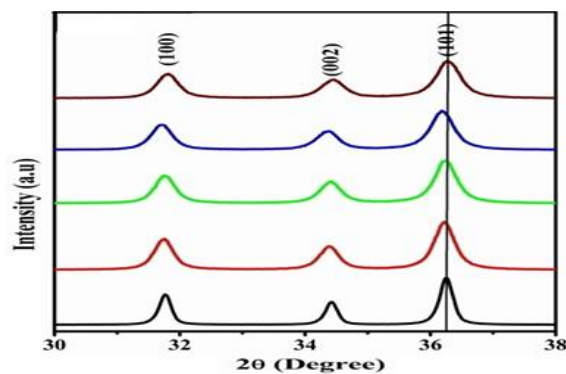
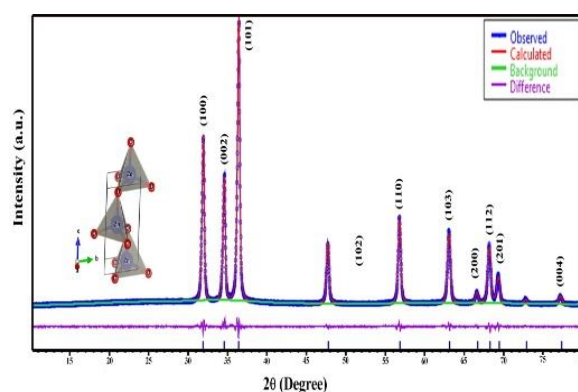


Fig. 1 (b) Enlarged XRD spectra of 2θ at 36° of $Zn_{1-x}Mn_xO$ ($x = 0.0, 0.01, 0.02, 0.03$ & 0.04) nanoparticles

Table 1. Structural parameters of pure ZnO and ZnO: Mn (1-4%) nanoparticles.

Sample	Pure ZnO	ZnO: Mn(1%)	ZnO: Mn(2%)	ZnO: Mn(3%)	ZnO: Mn(4%)
2θ	36.14	36.22	36.24	36.25	36.26
D (nm)	36.85	22.48	20.88	19.90	19.13
a (Å)	3.254	3.245	3.242	3.237	3.229
c (Å)	5.215	5.204	5.198	5.191	5.179
Volume	47.822	47.455	47.319	47.104	46.763
APF	0.7545	0.7540	0.7542	0.7540	0.7539
L (Å)	1.9806	1.9754	1.9734	1.9577	1.9657
c/a	1.603	1.604	1.604	1.604	1.604
δ (E^{-6})	736	1978	2293	2525	2732
S/V (E^{-4})	2606	2613	2616	2621	2627
Strain	0.0811	0.1327	0.1425	0.1496	0.1557

Fig. 2. Rietveld Refinement of $Zn_{1-x}Mn_xO$ ($x = 0.0$) nanoparticles.

3.2. Morphology and elemental analysis

Fig. 3 indicates the TEM micrograph of (a) $Zn_{1-x}Mn_xO$ ($x = 0.00$) and (b) $Zn_{1-x}Mn_xO$ ($x = 0.02$) nanoparticles and reveals that the synthesized samples are nearly spherical in shape with uniform size distribution.

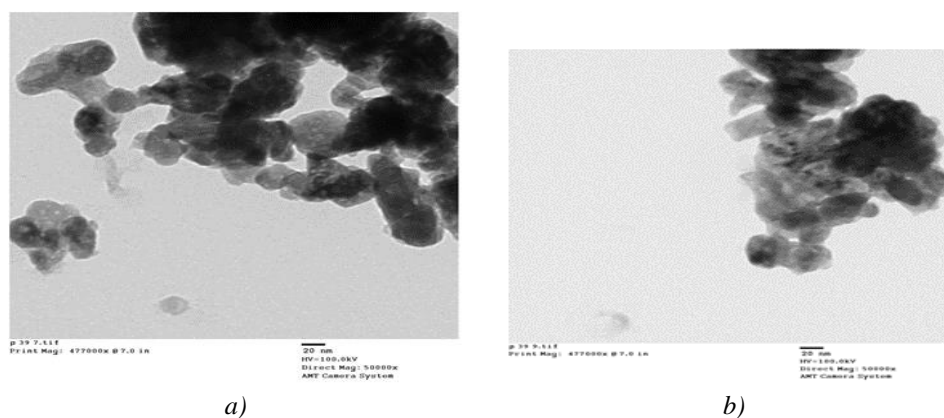
Fig. 3 TEM micrograph of $Zn_{1-x}Mn_xO$ nanoparticles: a) $x = 0.0$, b) $x = 0.02$

Fig. 4 (a)-(e) represents the FESEM micrographs of $Zn_{1-x}Mn_xO$ ($x = 0.0, 0.01, 0.02, 0.03$ & 0.04) nanoparticles. It indicates that, the synthesized nanoparticles are uniform spherical shape without agglomeration and the size ranges of 19 - 27 nm (from image -J software) depending upon the doping concentration which is well agreed with the size obtained from Debye Scherrer's formula. The chemical compositions of the samples were analyzed by Energy dispersive electron spectroscopy (EDAX), the corresponding spectrum and elemental percentages are shown in Fig. 5 (a)-f. It confirms the presence of only constituents such as Mn, Zn, and Oxygen in the samples without any impurities.

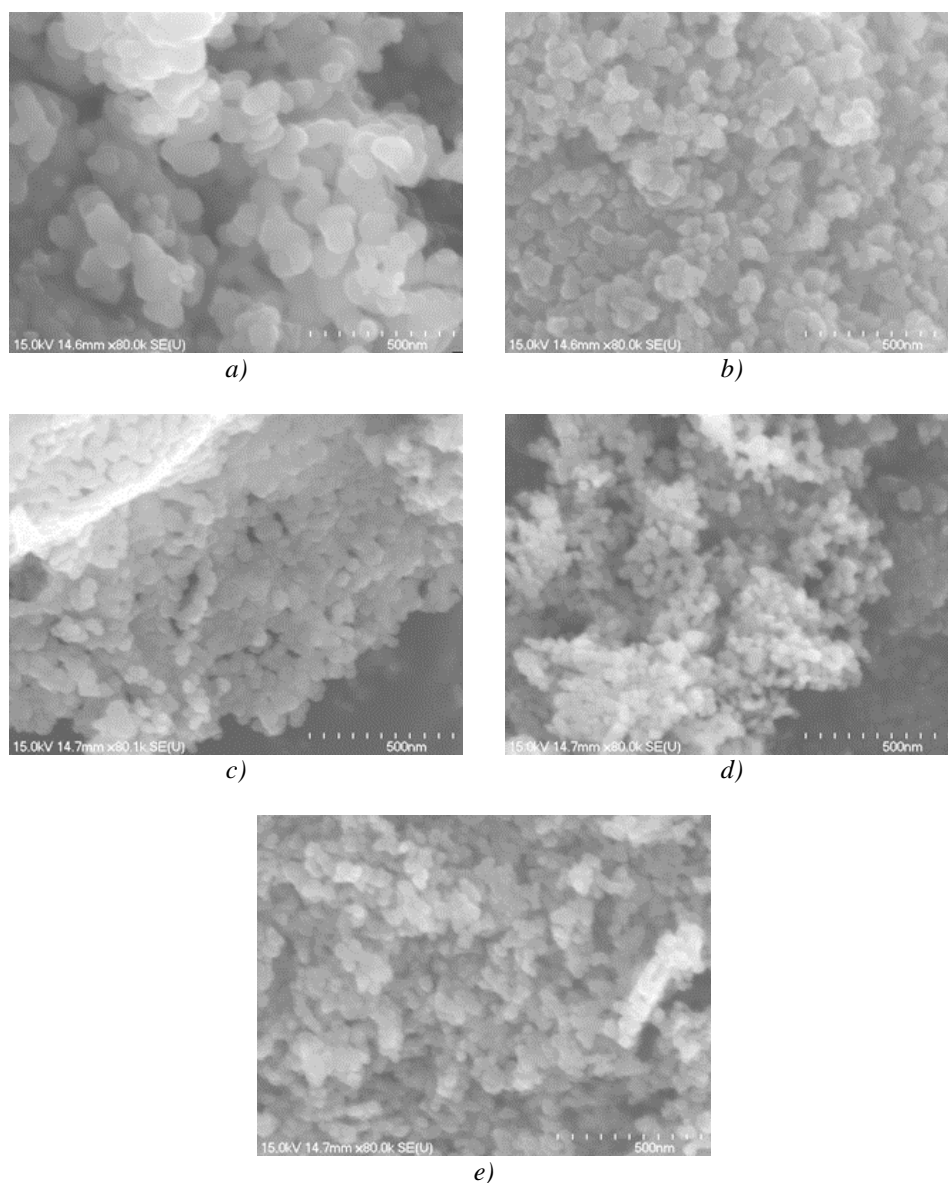


Fig. 4. (a) FESEM micrograph of $Zn_{1-x}Mn_xO$ nanoparticles
a) $x = 0.0$, b) $x = 0.01$, c) $x = 0.02$, d) $x = 0.03$, e) $x = 0.4$

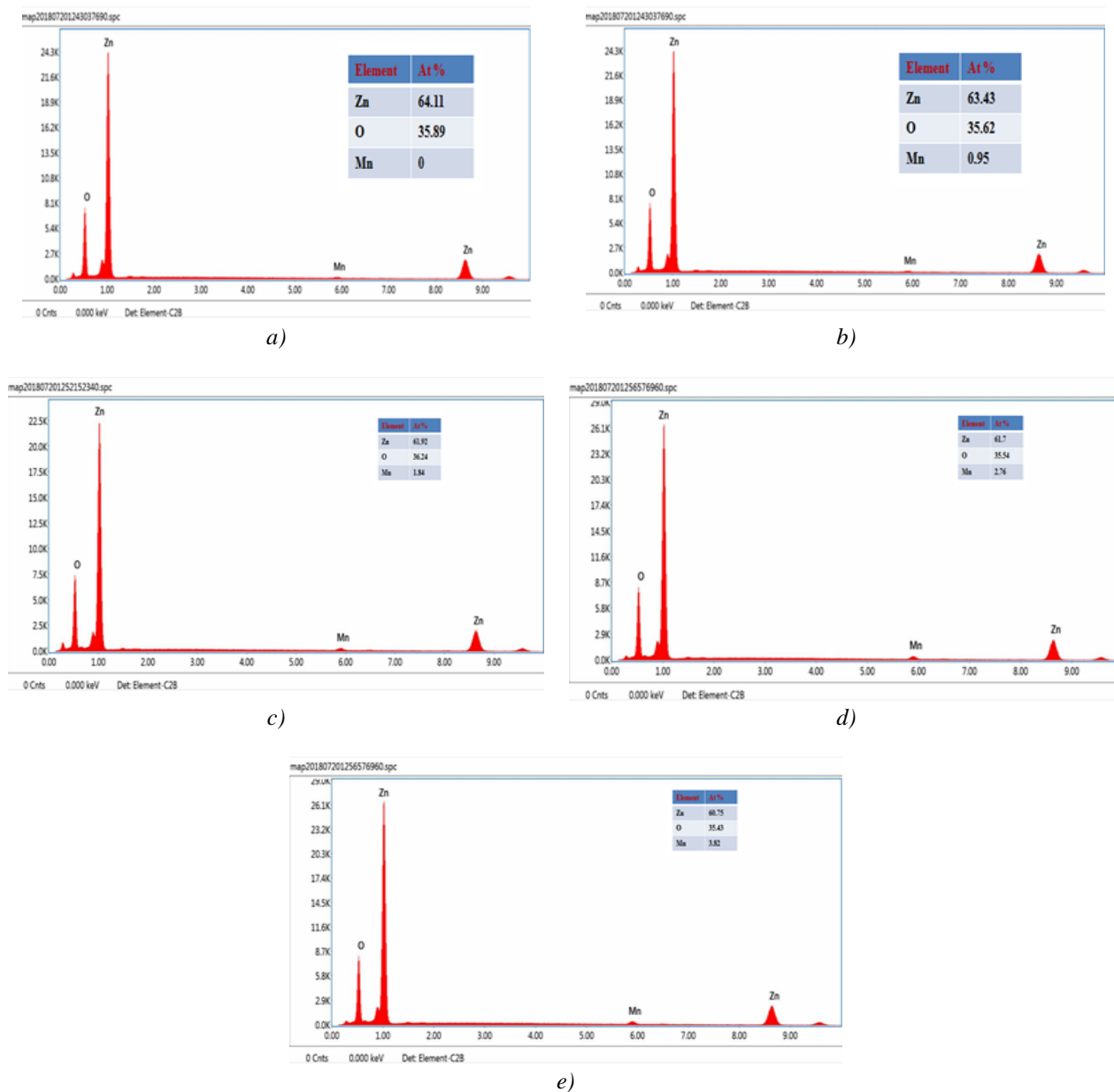


Fig. 5. EDAX spectrum of $Zn_{1-x}Mn_xO$ nanoparticles
 a) $x = 0.0$, b) $x = 0.01$, c) $x = 0.02$, d) $x = 0.03$, e) $x = 0.04$

3.3. DRS studies

The room temperature Diffusion Reflectance spectra (DRS) of $Zn_{1-x}Mn_xO$ ($x = 0.0, 0.01, 0.02, 0.03$ & 0.04) nanoparticles are shown in Fig. 6. From this figure it is observed that a sharp fall in reflectance at wavelengths of 377.99, 369.98, 367.77, 366.70, 365.36 nm were noticed for $Zn_{1-x}Mn_xO$ ($x = 0.0, 0.01, 0.02, 0.03$ & 0.04) nanoparticles respectively.

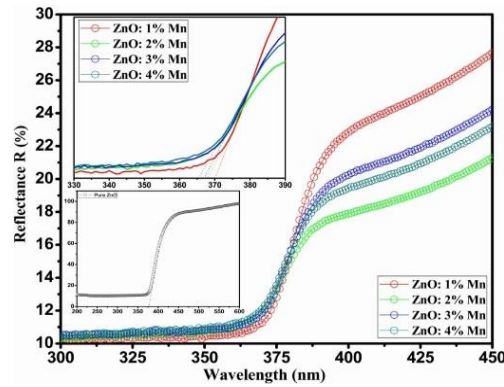


Fig. 6. DRS spectra of $Zn_{1-x}Mn_xO$ ($x = 0.0, 0.01, 0.02, 0.03$ & 0.04) nanoparticles and inset figure shows the $Zn_{1-x}Mn_xO$ ($x = 0.0$) nanoparticles.

Table 2. Size and Strain values of pure ZnO and ZnO: Mn (1-4%) nanoparticles from W-H plots.

Sample	D (nm)	Strain
Pure ZnO	36.57	0.0012
ZnO: Mn (1%)	24.12	0.0047
ZnO: Mn (2%)	21.39	0.0023
ZnO: Mn (3%)	20.84	0.0038
ZnO: Mn (4%)	19.76	0.0031

The corresponding energy gap (E_g) values are estimated by using the formula $E_g = 1240 / \lambda_{ex}$ and are observed as 3.28, 3.35, 3.37, 3.38, 3.39 eV respectively, and noted in the Table- 2. The energy band gap is found to be increase from 3.35 to 3.39 eV with Mn substitution in the ZnO host. This indicates a clear blue shift and could be attributed to the Moss-Burstein shift and this variation concurrence with the strain data related to structural change [36].

3.4. Raman analysis

Raman spectra of $Zn_{1-x}Mn_xO$ ($x = 0.0, 0.01, 0.02, 0.03$ & 0.04) nanoparticles measured in the range of $150 - 1500 \text{ cm}^{-1}$ are depicted in the Fig. 7 and corresponding modes are noticed in Table 3. From Fig. 7 it is observed that the peaks at $272, 384, 506, 608 \text{ cm}^{-1}$ are absent by Mn substitution. This mode has intensity considerably decreased in all doped samples. It may be due to the breaking of translational crystal symmetry by the incorporation of Mn. The E_2H peak at 438 cm^{-1} becomes broadened, and shifts towards 426 cm^{-1} (lower energies) with increase of Mn dopant. This broadening and shifting may be due to strain induced by Mn dopant. In Fe doped ZnO same trend was observed [38]. The $2L_{AM}$ mode shifted towards lower wave number from 327 to 316 cm^{-1} and A_1LO/E_1LO mode (595 cm^{-1}) also shifted towards lower as Mn concentration increases in the ZnO host. This may be due to defect activated Raman scattering phonon modes (DARS). i.e. It may attribute to the scattering contribution of A_1LO/E_1LO branches outside the B zone centres [8]. This might be associated with oxygen and zinc vacancies interstitials and other defects induced by TM ions. The concentration of these defects increases with increasing Mn concentration as shown by the increase intensity of E_1LO / A_1LO phonon mode at 575 cm^{-1} . Bundesmann, et al., [39] have already observed the same additional vibrational modes for different dopants. They suggest that, these modes are associated to defect induced modes that can be used as an index to test the dopant incorporation in the host matrix. In the same way, the vibrational mode at 575 cm^{-1} can be associated with Mn^{+2} impurities. This may be explained by the larger ionic radius of Mn^{+2} (0.66 \AA) compared to Zn^{+2} ionic radius (0.60 \AA). When Mn^{+2} substitute the Zn^{+2} ions, new lattice defects

are created or intrinsic host defects are activated. This presumption is in good agreement with the increasing intensity of E_1LO/A_1LO mode.

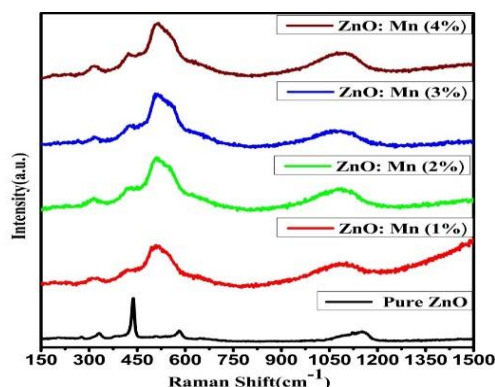


Fig. 8. Photoluminescence spectra of $Zn_{1-x}Mn_xO$ ($x = 0.0, 0.01, 0.02, 0.03$ & 0.04) nanoparticles.

Table 3. Optical bandgap values of pure ZnO and ZnO: Mn (1-4%) nanoparticles.

S. No.	Sample	λ (nm)	Eg (eV)
1	Pure ZnO	377.99	3.28
2	ZnO: Mn(1%)	369.98	3.35
3	ZnO: Mn(2%)	367.77	3.37
4	ZnO: Mn(3%)	366.70	3.38
5	ZnO: Mn(4%)	365.36	3.39

3.5. Photoluminescence (PL) analysis.

To study the impact of Mn on the PL of ZnO, the room temperature PL measurements were carried out at an excitation wavelength of 425 nm as shown in Fig. 8. From this figure, the emission peaks are observed at 465, 485, 507, 589, 624, 664 nm both in $Zn_{1-x}Mn_xO$ ($x = 0.0, 0.01, 0.02, 0.03$ & 0.04) nanoparticles. The luminescent properties of Mn^{+2} actuators have been studied by many researchers [6]; it mainly depends on the crystal structure of the host material. All the doped samples show a dominant peak at 465 nm, the PL intensity of all samples decreases with increase of Mn concentration in ZnO host. In general ZnO has two emissions located in the UV and visible regions [40]. The former is associated to the near band edge emission through exciton-exciton radiative recombination and the later emission, is due to the defects, mainly oxygen related vacancies are most favorable for visible emission [41]. FM ordering is directly linked to the dopant concentration and oxygen vacancies [42].

The blue band emission peak at 465 nm is associated to surface defects such as oxygen vacancies (V_o), and zinc interstitials (Zn_i) due to electronic transition between Zn_i level to the valance band [43]. The blue green emission at 485 nm is possibly due to surface defects in ZnO Nanoparticles. It can be attributed to the transition between oxygen vacancy (V_o) to oxygen interstitial (O_i) [44]. Oxygen vacancies are responsible for green emission at 507 nm may originate from recombination of V_o^+ with photo generated holes [43]. The yellow emission band at 589 nm is associated to doubly charged oxygen vacancy (V_o^{++}) [42]. In ZnO: Mn, V_o^+ with an unpaired electron may be responsible for FM in pure and Mn doped ZnO. The M_s of $Zn_{1-x}Mn_xO$ ($x = 0.02$) nanoparticles, it is not only related to V_o^+ concentration but also to the Mn^{+2} concentration in the ZnO lattice. The green yellow peak at 589 nm represent the defect complexes of V_o and Zn_i [44] mainly, it is assigned to the transition between the unpaired oxygen vacancy and the photo excited hole in the valance band of ZnO [45]. The peaks at 624, 664 nm are due to the monovalent

vacancy of oxygen or zinc and dually ionized oxygen vacancies respectively [46]. The peak intensity decreases with Mn concentration may be due to the decreased particle size.

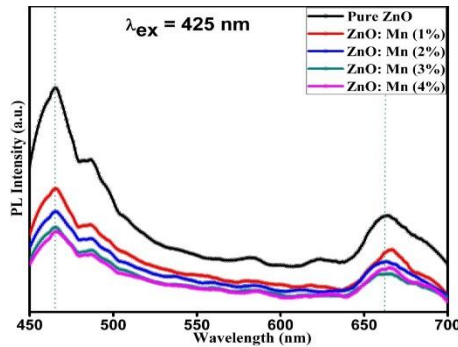


Fig. 8. Photoluminescence spectra of $Zn_{1-x}Mn_xO$ ($x = 0.0, 0.01, 0.02, 0.03$ & 0.04) nanoparticles.

3.6. Magnetization analysis

Magnetization measurements of $Zn_{1-x}Mn_xO$ ($x = 0.0, 0.01, 0.02, 0.03$ & 0.04) nanoparticles were performed using Vibrating sample magnetometer at room temperature. Fig. 9 depicts the positive s type hysteresis loop obtained from the magnetization versus applied field (H) data. It reflects that all the samples are ferromagnetic at room temperature with certain values of H_c , M_s and M_R are tabulated in the Table 4.

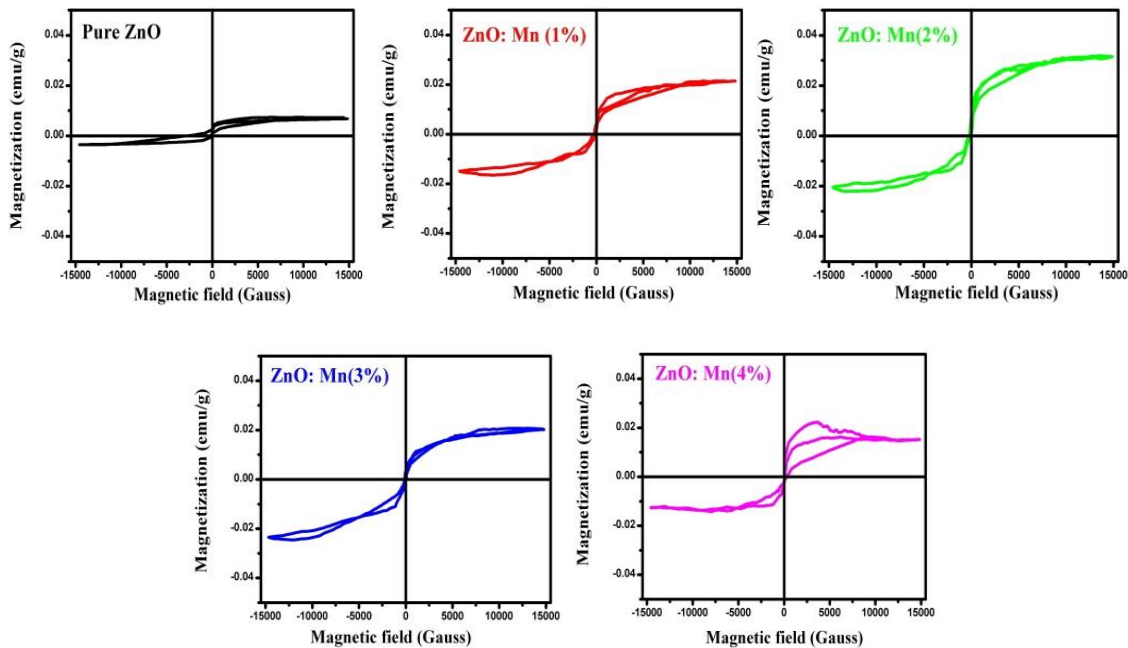


Fig. 9. M - H hysteresis loops of $Zn_{1-x}Mn_xO$ ($x = 0.0, 0.01, 0.02, 0.03$ & 0.04) nanoparticles.

Though numerous work has been developed on the TM doped ZnO, the mechanism responsible for the extraction of RTFM in TM doped ZnO still remains controversial. So far many researchers believed that the origin of RTFM attributes to the role of secondary phase/impurity phase [47, 48]. But for our samples the RTFM may not derive from any impurity phase, because no impurity peak was detected from XRD results. Researchers considered RTFM arose due to the

interaction between Mn^{+2} ions and defects [47, 48]. In our samples XRD and Raman results indicates a number of defects present in the synthesized nanoparticles. FM in ZnO nanoparticles is stimulated by doping of TM (Mn), which replaces the Zn ions on doping. Due to the high concentration of spinning electrons in manganese, ferromagnetic exchange interactions occurred between Mn ions and oxygen ions that results in the initiation of ferromagnetism into Mn substituted ZnO nanoparticles. The exchange interaction is due to the overlap of 3d orbital electrons with oxygen vacancies or interstitial Zn atoms in ZnO nanoparticles [4]. Hence the RTFM arises as a result of exchange interaction between the free localized charge carriers initiating from the oxygen vacancies and Zn interstitials in the crystal structure as a result of doping [49, 50]. The exchange interactions between the defects and surrounding Mn^{+2} ions form a BMP (Bound Magnetic Polaron). Neighboring BMPs may overlap and results in the long range Mn^{+2} - Mn^{+2} ferromagnetic coupling in DMS. As Mn concentration increases the concentration of defects has also increases, hence more BMPs will be formed and may overlap. The presence of high oxygen vacancy concentration in the sample gives rise to ferromagnetic ordering. Thus the presence of more oxygen vacancies may have resulted in the increment of magnetization for $Zn_{1-x}Mn_xO$ ($x = 0.01, 0.02, 0.03$ & 0.04). Further high M_s is observed in $Zn_{1-x}Mn_xO$ ($x = 0.02$) than $x = 0.01$, meanwhile the increase of Mn concentration may lead to form Mn cluster in ZnO matrix. ZnO: Mn nanoparticles have a tendency to form a cluster as the surface to volume ratio is very high. In Mn cluster the interactions between neighboring Mn^{+2} ions are antiferromagnetic and decrease the overall ferromagnetic order in Mn doped ZnO samples [47, 48]. This may be the reason for decrease of M_s in $Zn_{1-x}Mn_xO$ ($x = 0.03$ and 0.04). Bououdina et al. [4] also reported the same type of behaviour in TM doped ZnO. It was reported theoretically, that the FM behavior in doped ZnO arises from the holes concentration, possibly ascribed to their strong p-d exchange interaction between the acceptor level Zn^{+2} and the donor level Mn^{+2} [34]. Dietl et al predicted that Mn doped p-type ZnO should be ferromagnetic at room temperature. In the absence p-type doping, theoretical calculations predicted that Mn doped ZnO would exhibit AFM property [19]. According to BMP model the magnetic properties of Mn doped ZnO could be tuned through Mn and defect concentration. From the Table 4, it is observed that, the M_s increases from 0.022 to 0.033 emu/g as the Mn concentration increases and further decreased magnetization. Among them, $Zn_{1-x}Mn_xO$ ($x = 0.02$) has highest M_s which is the promising candidate for the spintronics applications.

Table 4. Magnetization parameters of pure ZnO and ZnO: Mn (1-4%) nanoparticles.

S. No.	Sample	H_c (G)	M_s (emu/g)	M_R (emu/g)	SQR
1	Pure ZnO	2842.5	0.0071	0.0026	0.173
2	ZnO: Mn(1%)	227.5	0.022	0.0045	0.204
3	ZnO: Mn(2%)	162.5	0.033	0.0062	0.189
4	ZnO: Mn(3%)	124.64	0.021	0.0033	0.157
5	ZnO: Mn(4%)	117.6	0.015	0.0025	0.167

4. Conclusions

In conclusions, $Zn_{1-x}Mn_xO$ ($x = 0.0, 0.01, 0.02, 0.03$ & 0.04) nanoparticles were synthesized by simple chemical combustion method. Both XRD and Raman spectroscopy studies designated the effective substitution of Mn ions into the ZnO host lattice. A blue shift was detected in the reflectance spectra of the ZnO Nanoparticles owing to Mn doping concentration. The PL spectra of all the Nanoparticles displayed the similar emissions and decreased PL intensity with the increase in Mn content.

All the Nanoparticles showed typical ferromagnetism at room temperature, although, the $Zn_{1-x}Mn_xO$ ($x = 0.02$) nanoparticles exhibited better FM property than remaining samples. These

interesting optical, photoluminescence and magnetic properties of the $Zn_{1-x}Mn_xO$ ($x = 0.02$) nanoparticles may find applications in both spintronic and optoelectronic applications.

References

- [1] N. Rajamanickam, S. Rajashabala, K. Ramachandran, *Journal of Luminescence* **146**, 226(2014).
- [2] M. Saleem, S. Atiq, S. M. Ramay, A. Mahmood, S. A. Siddiqi, M. A. Shar, *Advances in Materials Science and Engineering* **2014**, 1 (2014).
- [3] M. Fang, C. M. Tang, Z. W. Liu, *Journal of Electronic Materials* **47**, 1390 (2018).
- [4] K. Jayanthi, S. Chawla, K. N. Sood, M. Chhibara, S. Singh, *Applied Surface Science* **255**, 5869 (2009).
- [5] Y. Ohno, D. K. Young, B. A. Beschoten, F. Matsukura, H. Ohno, D. D. Awschalom, *Nature* **402**, 790 (1999) .
- [6] C. Jing, Y. Jiang, W. Bai, J. Chu, A. Liu, *Journal of magnetism and magnetic materials* **322**, 2395 (2010).
- [7] A. J. Reddy, M. K. Kokila, H. Nagabhushana, J. L. Rao, B. M. Nagabhushana, C. Shivakumara, R. P. Chakradhar, *Spectrochimica Acta Part A: Molecular and Biomolecular Spectroscopy* **79**, 476 (2011).
- [8] S. Rasouli, S. J. Moeen, *Journal of Alloys and Compounds* **509**, 1915 (2011).
- [9] N. Sharma, R. Kant, V. Sharma, S. Kumar, *Journal of Electronic Materials* **47**, 4098 (2018).
- [10] M. Venkatesan, C. B. Fitzgerald, J. G. Lunney, J. M. Coey, *Physical review letters* **93**, 177206 (2004).
- [11] R. Viswanatha, S. Sapra, S. Sen Gupta, B. Satpati, P. V. Satyam, B. N. Dev, D. D. Sarma, *The Journal of Physical Chemistry B* **108**, 6303 (2004).
- [12] W. Zaets, K. Ando, *Applied Physics Letters* **77**, 1593 (2000).
- [13] X. M. Cheng, C. L. Chien, *Journal of Applied Physics* **93**, 7876 (2003).
- [14] S. J. Han, T. H. Jang, Y. B. Kim, B. G. Park, J. H. Park, Y. H. Jeong, *Applied Physics Letters* **83**, 920 (2003).
- [15] T. Fukumura, Z. Jin, M. Kawasaki, T. Shono, T. Hasegawa, S. Koshihara, H. Koinuma, *Applied Physics Letters* **78**, 958 (2001).
- [16] C. J. Cong, L. Liao, Q. Y. Liu, J. C. Li, K. L. Zhang, *Nanotechnology* **17**, 1520 (2006).
- [17] J. Alaria, P. Turek, M. Bernard, M. Bouloudenine, A. Berbadj, N. Brihi, G. Schmerber, S. Colis, A. Dinia, *Chemical Physics Letters* **415**, 337 (2005).
- [18] S. J. Pearton, C. R. Abernathy, D. P. Norton, A. F. Hebard, Y. D. Park, L. A. Boatner, J. D. Budai, *Materials Science and Engineering: R: Reports* **40**, 137 (2003).
- [19] K. Sato, H. Katayama-Yoshida, *Physica E: Low-dimensional Systems and Nanostructures* **10**, 251 (2001).
- [20] S. J. Han, T. H. Jang, Y. B. Kim, B. G. Park, J. H. Park, Y. H. Jeong, *Applied Physics Letters* **83**, 920 (2003).
- [21] K. R. Kittilstved, D. R. Gamelin, *Journal of the American Chemical Society* **127**, 5292 (2005).
- [22] D. Rubi, J. Fontcuberta, A. Calleja, L. Aragonés, X. G. Capdevila, M. Segarra, *Physical Review B* **75**, 155322 (2007).
- [23] M. Venkatesan, C. B. Fitzgerald, J. M. Coey, *Nature* **430**, 630 (2004).
- [24] C. C. Lin, Y. Y. Li, *Materials Chemistry and Physics* **113**, 334 (2009).
- [25] G. Vijayaprasath, R. Murugan, S. Asaithambi, P. Sakthivel, T. Mahalingam, Y. Hayakawa, G. Ravi, *Ceramics International* **42**, 2836 (2016).
- [26] C. J. Cong, L. Liao, J. C. Li, L. X. Fan, K. L. Zhang, *Nanotechnology* **16**, 981 (2005).
- [27] F. Achouri, S. Corbel, L. Balan, K. Mozet, E. Girod, G. Medjahdi, M. B. Said, A. Ghrabi, R. Schneider, *Materials & Design* **101**, 309 (2016).
- [28] J. H. Lee, B. O. Park, *Thin Solid Films* **426**, 94 (2003).
- [29] B. Panigrahy, M. Aslam, D. Bahadur, *The Journal of Physical Chemistry C* **114**, 11758 (2010).

- [30] S. Baruah, J. Dutta, *Science and Technology of Advanced Materials* **10**, 013001 (2009).
- [31] A. Abdel-Galil, M. R. Balboul, A. Sharaf, *Physica B: Condensed Matter* **477**, 20 (2015).
- [32] M. Ahmad, E. Ahmed, Y. Zhang, N. R. Khalid, J. Xu, M. Ullah, Z. Hong, *Current Applied Physics* **13**, 697 (2013).
- [33] P. Kadam, C. Agashe, S. Mahamuni, *Journal of Applied Physics* **104**, 103501 (2008).
- [34] K. Omri, J. El Ghoul, O. M. Lemine, M. Bououdina, B. Zhang, L. El Mir, *Superlattices and Microstructures* **60**, 139 (2013).
- [35] M. E. Abrishami, S. M. Hosseini, E. A. Kakhki, A. Kompany, M. Ghasemifard, *International Journal of Nanoscience* **9**, 19 (2010).
- [36] P. Bindu, S. Thomas, *Journal of Theoretical and Applied Physics* **8**, 123 (2014).
- [37] R. Loudon, *Proc. R. Soc. Lond. A* **275**, 218 (1963).
- [38] A. J. Reddy, M. K. Kokila, H. Nagabhushana, S. C. Sharma, J. L. Rao, C. Shivakumara, B. M. Nagabhushana, R. P. Chakradhar, *Materials chemistry and Physics* **133**, 876 (2012).
- [39] C. Bundesmann, N. Ashkenov, M. Schubert, D. Spemann, T. Butz, E. M. Kaidashev, M. Lorenz, M. Grundmann, *Applied Physics Letters* **83**, 1974 (2003).
- [40] T. Pandiyarajan, R. V. Mangalaraja, B. Karthikeyan, P. Sathishkumar, H. D. Mansilla, D. Contreras, J. Ruiz, *Applied Physics A* **119**, 487 (2015).
- [41] S. B. Rana, A. Singh, N. Kaur, *Journal of Materials Science: Materials in Electronics* **24**, 44 (2013).
- [42] Q. Gao, Y. Dai, C. Li, L. Yang, X. Li, C. Cui, *Journal of Alloys and Compounds* **684**, 669 (2016).
- [43] D. E. Motaung, I. Kortidis, D. Papadaki, S. S. Nkosi, G. H. Mhlongo, J. Wesley-Smith, G. F. Malgas, B. W. Mwakikunga, E. Coetsee, H. C. Swart, G. Kiriakidis, *Applied Surface Science* **311**, 14 (2014).
- [44] M. Silambarasan, S. Saravanan, T. Soga, *Physica E: Low-dimensional Systems and Nanostructures* **71**, 109 (2015).
- [45] H. V. Pessoni, L. J. Maia, Jr A. Franco, *Materials Science in Semiconductor Processing* **30**, 135 (2015).
- [46] J. X. Wang, X. W. Sun, Y. Yang, K. K. Kyaw, X. Y. Huang, J. Z. Yin, J. Wei, H. V. Demir, *Nanotechnology* **22**, 325704 (2011).
- [47] S. Kolesnik, B. Dabrowski, J. Mais, *Journal of superconductivity* **15**, 251 (2002).
- [48] J. H. Li, D. Z. Shen, J. Y. Zhang, D. X. Zhao, B. S. Li, Y. M. Lu, Y. C. Liu, X. W. Fan, *Journal of magnetism and magnetic materials* **302**, 118 (2006).
- [49] D. Gao, J. Zhang, G. Yang, J. Qi, M. Si, D. Xue, *The Journal of Physical Chemistry C* **115**, 16405 (2011).
- [50] S. Muthukumar, M. Ashokkumar, *Journal of Electronic Materials* **45**, 976 (2016).